Supporting Information for

Manipulating Protons and Oxygen Vacancies in Nickelate Oxides by Thermochemical Dehydration

Haowen Chen[a,b‡], Zihan Xu[a,b‡], Luhan Wei[b], Mingdong Dong[c], Yang Hu[b], Ying Lu[b], Nian Zhang[d], Jie Wu[c], and Qiyang Lu[b,e*]

[a.] Zhejiang University, Hangzhou 310027, China

[b.] School of Engineering, Westlake University, Hangzhou 310030, China

[c.] Key Laboratory for Quantum Materials of Zhejiang Province, School of Science, Westlake University, Hangzhou 310030, China

[d.] Shanghai Synchrotron Radiation Facility, Shanghai Advanced Research Institute, Chinese Academy of Sciences, Shanghai 201204, China

[e.] Research Center for Industries of the Future, Westlake University, Hangzhou 310030, Zhejiang, China

† Electronic supplementary information (ESI) available.

‡ These authors contributed equally to this work.

*Corresponding author: luqiyang@westlake.edu.cn

Structural characterizations of pristine $NdNiO_3$, protonated H_xNdNiO_3, and oxygen deficient $NdNiO_{3-\delta}$

2θ-ω scans of the (001) diffraction peak and the (002) diffraction peak of the pristine $NdNiO_3$ (denoted as NNO), protonated H_xNdNiO_3 (denoted as H-NNO), oxygen deficient $NdNiO_{3-\delta}$ are shown in Figure S1.

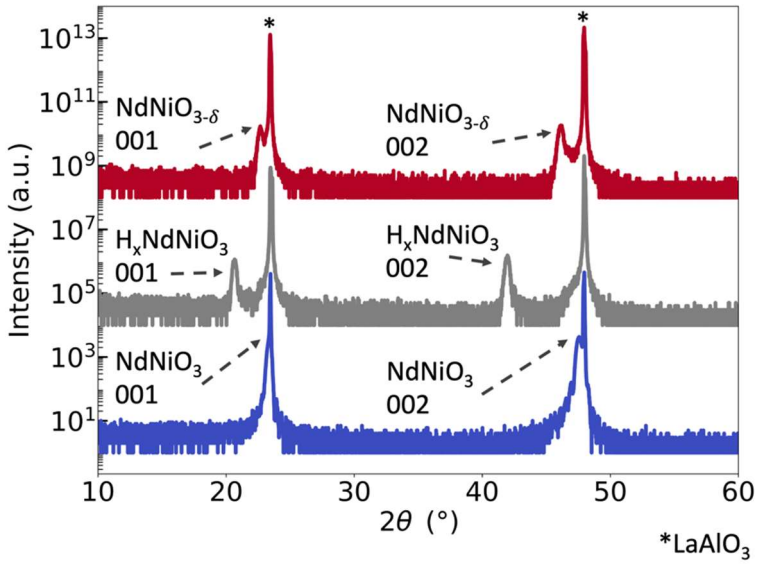

Figure S1. X-ray diffraction (XRD) 2θ-ω patterns of NNO, H-NNO, NNO-δ thin films grown on $LaAlO_3$ substrates in the 2θ range of 10°-60°.

X-ray diffraction rocking curves of NNO, H-NNO and NNO-δ

The full-width half maximum (FWHM) of pristine NNO is ~ 0.06° (Figure S2a). Figure S2b&c shows the FWHM of rocking curves of protonated H-NNO and oxygen deficient NNO-δ is roughly the same, which is comparable with the pristine NNO. The narrow width of rocking curves of the latter two samples indicates that they have equally good crystal quality.

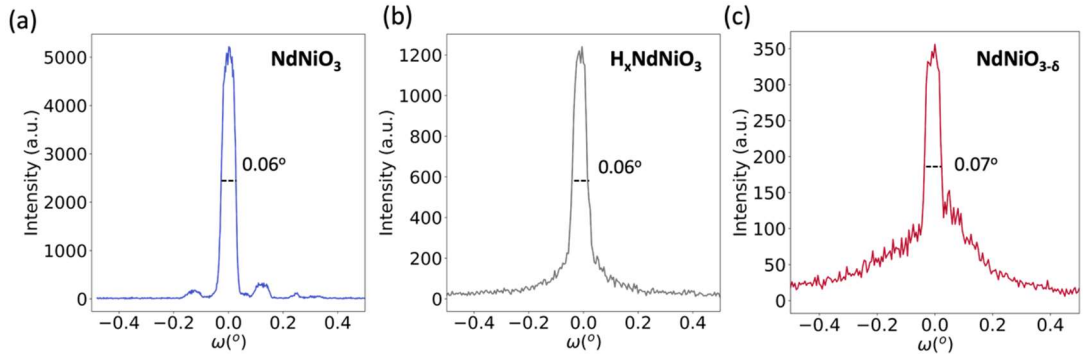

Figure S2. (a) The rocking curve of the NNO thin film, (b) The rocking curve of the H-NNO thin film, (c) The rocking curve of the NNO-δ thin film.

Structural evolution of NNO-δ under different conditions

We have characterized the crystal structure of NNO-δ under different ambient conditions. We first annealed the oxygen deficient sample in a pure O_2 atmosphere at 300°C. We found that the NNO-δ phase can restore to the pristine NNO without oxygen deficiency, as shown in Figure S3a. We further investigated the dehydration of protonated H-NNO to NNO-δ under different reducing atmospheres. Figure S3b shows the XRD patterns NNO-δ forming in different reducing atmospheres. Here, the humid condition refers to an atmosphere containing 3% H_2O, and the mix of H_2 and N_2 gas has a volume ratio of 5%: 95%. The lattice constant of NNO-δ recorded as $c_{pc,\ NNO\text{-}\delta}$ = 3.92 Å, remains consistent across different reducing atmospheric conditions. We also tested the structure of stability of NNO-δ sample in different reducing atmospheres at temperatures higher than 300°C as shown in Figure S3c. 2θ-ω XRD patterns reveal that NNO-δ undergoes a reversible phase transition back to the NNO phase when exposed to a humid N_2 atmosphere at 500°C. In contrast, the crystal structure of NNO-δ degrades to an amorphous structure at the same temperature under humid H_2 at 500°C.

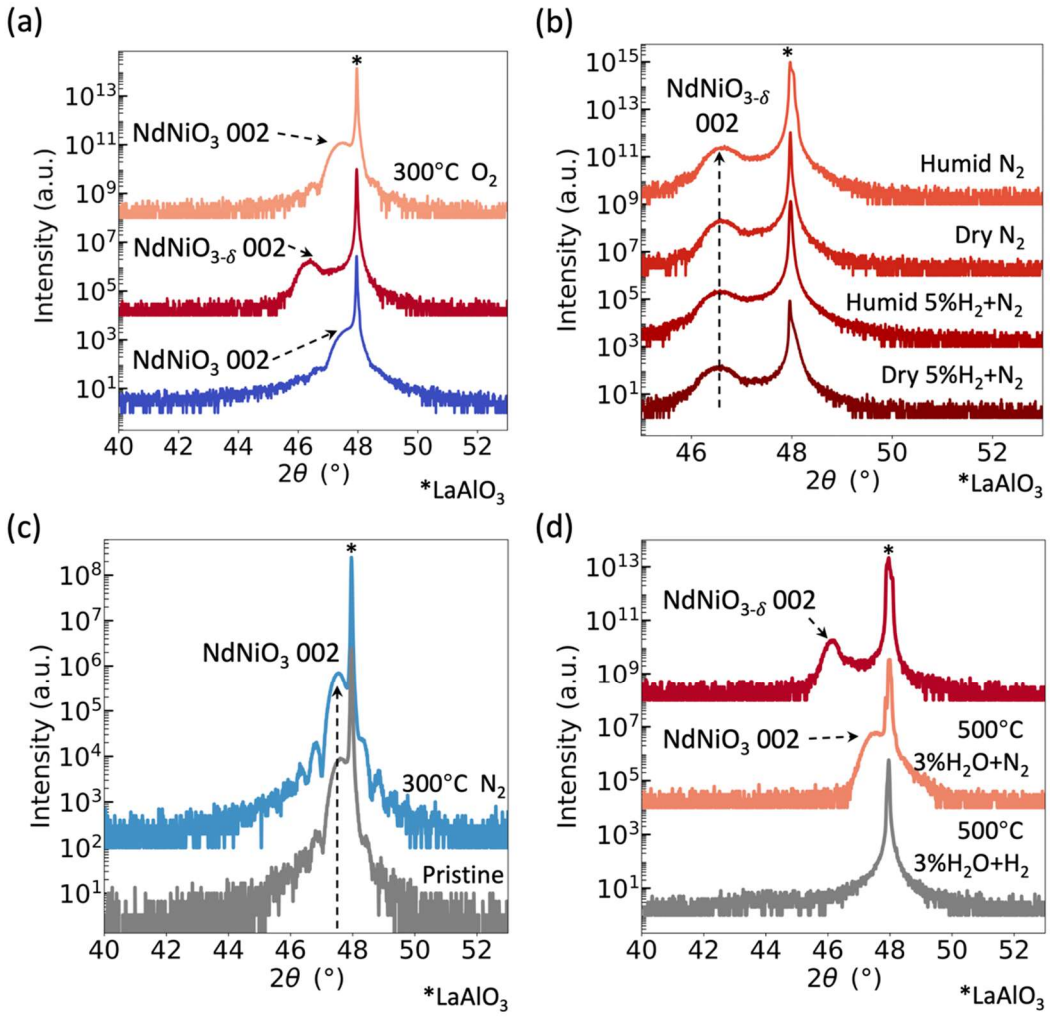

Figure S3. (a) Structural characterizations of NNO-δ under pure O_2 atmosphere. *2θ-ω* XRD patterns of pristine NNO (blue), NNO-δ (red), NNO after annealing in O_2 (orange). (b) Structural characterizations of NNO-δ formed in different reducing atmospheres. *2θ-ω* XRD patterns show the structure of NNO-δ formed at 300°C in four different reducing atmospheres: humid N_2, dry N_2, humid mixture of H_2 and N_2 and dry mixture of H_2 and N_2. (c) Stability of NNO-δ at high temperature in different reducing atmospheres. The oxygen deficient NNO-δ sample was annealed at 500°C in humid N_2 (orange) and humid H_2 (grey) atmospheres, respectively.

Fitting of soft X-ray adsorption spectra of NNO, H-NNO, NNO-δ, NiO

We used two Gaussian peaks for fitting the soft X-ray adsorption spectra (sXAS) of NNO, H-NNO, NNO-δ and NiO, as shown in Figure S4. Figure S4a shows the two peaks were used for fitting the Ni L_3-edge sXAS in pristine NNO. The feature peak A is centered at ~854.5 eV and the feature peak B is centered at ~856 eV. Similar feature peaks are observed in the Ni L_3-edge of NNO-δ, H-NNO, and NiO (Figure S4b&c&d). The green Gaussian component represents the feature peak A. The yellow Gaussian component represents the feature peak B. The area ratio compared between feature peak A and feature peak B can be used as a reference to calculate the Ni valence state. The Ni valence state of H-NNO and NNO-δ is close to Ni^{2+} due to their area $ration_{(B/A)}$ is close to the area $ration_{(B/A)}$ of NiO.

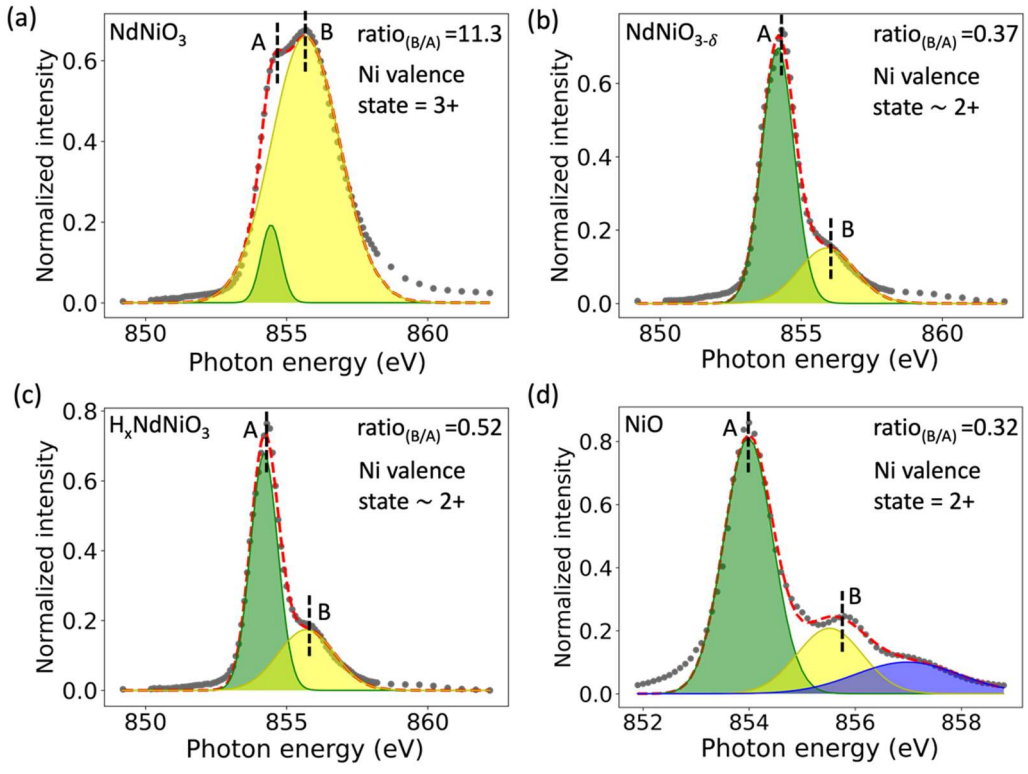

Figure S4. Fitting results of the Ni L_3-edge sXAS measured on (a) NNO, (b) NNO-δ, (c) H-NNO (d) NiO samples.

Temperature-dependent electrochemical impedance spectroscopy and equivalent circuit analysis

The electrochemical impedance spectroscopy (EIS) was carried out in a humid atmosphere (pH_2O: pN_2 = 3%:97%) while heating the sample from 50°C to 300°C. This method allows for the observation of changes in electrical impedance associated with the phase transition from H-NNO to NNO-δ (Figure S5a). Figure S5b shows the equivalent circuit analysis of the EIS result. The model comprises a resistor (R_0, which represents the resistance from the wires used for measurements, and/or other sources of contact resistance) in series with a parallel configuration that includes a resistor (R_1, which represents the resistance of the H-NNO/NNO-δ thin films) and a constant phase element (CPE_1, most likely due to the stray capacitance from the wires used).

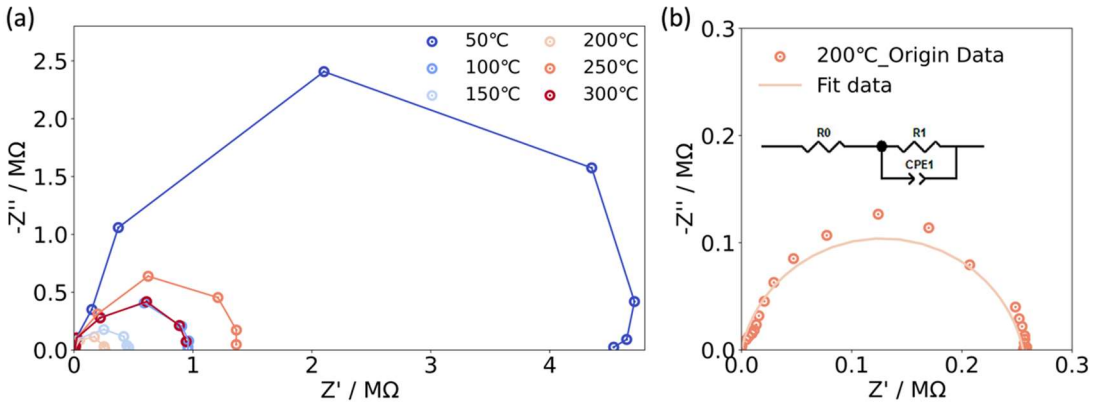

Figure S5. (a) Temperature-dependent Nyquist plots (real part of impedance $Z^{'}$ ~ imaginary part $Z^{''}$) of the impedance spectra of the phase transition in H-NNO to NNO-δ. (b) Equivalent circuit modeling for impedance spectra analysis.

The out-of-plane lattice constant of proton graded H-NNO thin film and oxygen vacancy graded NNO-δ thin film

We concluded the out-of-plane lattice constant of both H-NNO thin film with proton concentration gradient and NNO-δ thin film with oxygen vacancy concentration gradient in Figure S6a and Figure S6b , respectively. Figure S6a shows the protonation process happens in two different stages. From 0 mm to 2.5mm, the proton concentration is low, and the lattice constant of NNO slightly expands from 3.81 Å to 3.84 Å. Once the proton concentration reaches the threshold value, the H-NNO phase with a lattice constant at 4.31 Å forms. From 2.5 mm to 5 mm, a two-phase region exists. Figure S6b shows the dehydration of the graded H-NNO thin film happened in two different stages. From 0 mm to 2.5 mm, dehydration of the NNO phase with low proton concentration induces the oxygen deficient phase NNO-δ with a lattice constant of $c_{pc,\ NNO\text{-}\delta}$ = 3.87 Å. On the other hand, from 2.5 mm to 5 mm, dehydration of H-NNO with a higher proton concentration resulted in the oxygen deficient phase NNO-δ with a changing lattice constant $c_{pc,\ NNO\text{-}\delta}$ between 3.87 Å and 3.91 Å.

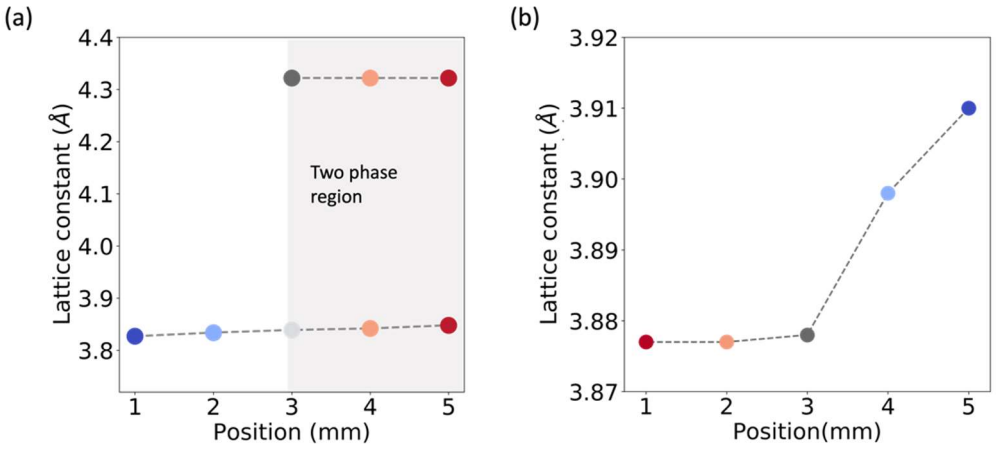

Figure S6. (a) The out-of-plane lattice constant of proton concentration gradient thin film extracted from Figure 4a at each spot of the thin film. (b) The out-of-plane lattice constant of oxygen vacancy concentration gradient thin film extracted from Figure 4b at each spot of the thin film.

Peak fitting results of Ni L_3-edge of proton graded H-NNO thin film and oxygen vacancy graded NNO-δ thin film

We continuously used two Gaussian peaks to fit the Ni L_3-edge of H-NNO thin film with proton concentration gradient and NNO-δ thin film with oxygen vacancy concentration gradient. We concluded the fitting results of the Ni L_3-edge at different positions of the H-NNO and NNO-δ thin film in Figure S7a and Figure S7b, respectively. In both Figure S7a&b, the green Gaussian component represents the feature peak A (centered at ~854.5 eV) and the yellow Gaussian component represents the feature peak B (centered at ~856 eV), which is the same as previous results in Figure S4. We also calculated the area ratio$_{(B/A)}$ of each spot of the H-NNO and NNO-δ thin film as shown in Figure S7c. Using the area ratio$_{(B/A)}$ of NNO and NiO as a reference, we can calculate the Ni valence state change of both proton graded H-NNO thin film and oxygen vacancy graded NNO-δ thin film.

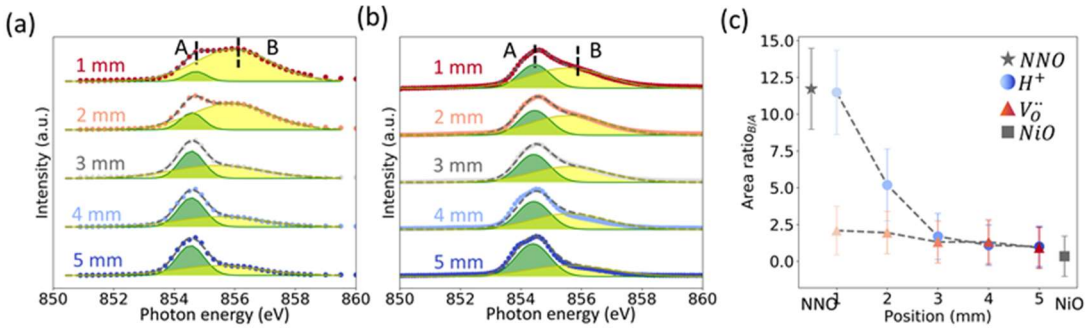

Figure S7. (a) Peak fitting results of Ni L_3-edge of H-NNO thin film with a proton concentration gradient. (b) Peak fitting results of Ni L_3-edge of NNO-δ thin film with a gradient of oxygen vacancy concentration. (c) Area ratio$_{(B/A)}$ of each spot of the H-NNO and NNO-δ thin film. The blue gradient spot is the thin film along the proton concentration gradient. The red gradient spot is the thin film along the oxygen vacancy concentration gradient.

O *K*-edge sXAS of proton graded H-NNO thin film and oxygen vacancy graded NNO-δ thin film

The oxygen vacancy concentration gradient sample was synthesized by annealing the proton gradient sample a in an N_2 atmosphere. The pre-edge peak at 530 eV in both Figure S8a&b represents the hybridization between the Ni *3d* orbital and the O *2p* orbital[1]. For both proton defects and oxygen vacancies, the formation of defects induces electron doping, which suppresses the pre-edge peak.

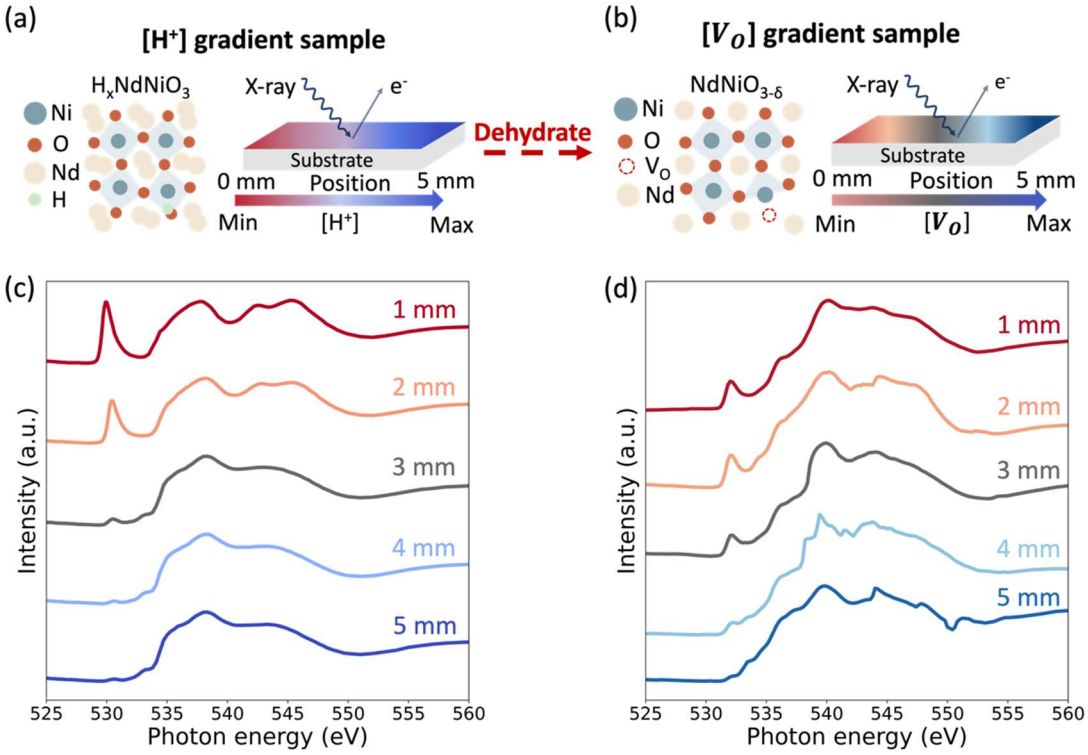

Figure S8. (a) Schematic showing sXAS with the spatial resolution to characterize the Ni valence state of the H-NNO thin film. (b) Schematic showing sXAS with the spatial resolution to characterize the Ni valence state of the NNO-δ thin film. (c) O *K*-edge of the protonated H-NNO thin film sample with the proton concentration gradient. (d) O *K*-edge of the oxygen deficient NNO-δ thin film sample with oxygen vacancy concentration gradient.

Structural characterizations of proton graded H-NNO thin film and the same sample after annealing in a pure H_2 atmosphere

We annealed the H-NNO thin film with proton concentration gradient in a pure H_2 atmosphere at 300°C. The oxygen vacancy concentration in the H_2 annealed sample is homogenous. The lattice constant is $c_{pc,\ NNO\text{-}\delta}$ = 3.94 Å and remains consistent throughout the entire thin film.

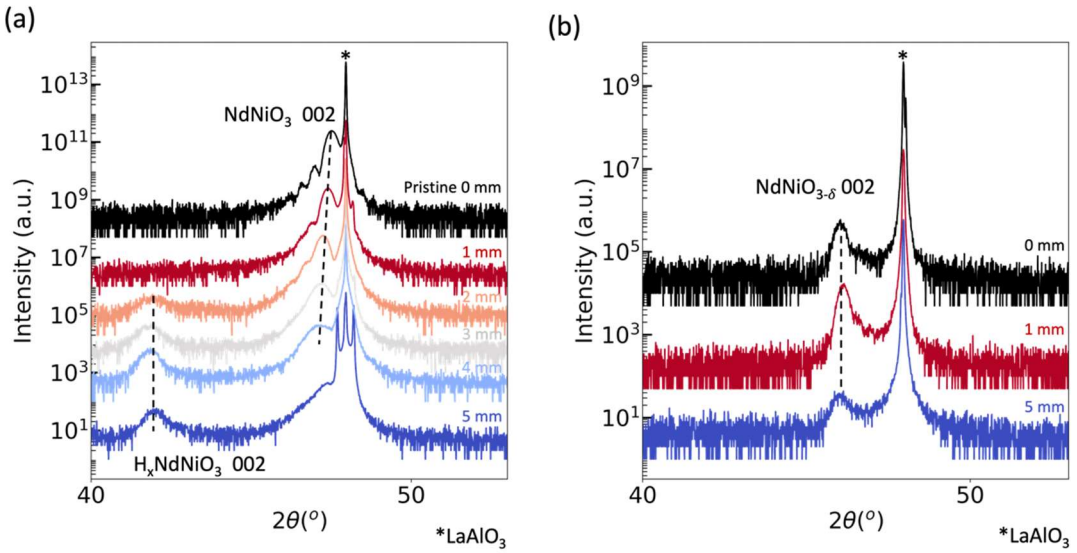

Figure S9. (a) *2θ-ω* XRD patterns of the thin film along the proton concentration gradient. (b) *2θ-ω* XRD patterns for identical locations on the thin film as specified in a, detailing the diffraction characteristics corresponding to each spot.

Non-stochiometry at different position of the concentration gradient thin film

we have plotted the non-stoichiometry (i.e., hydrogen non-stoichiometry x as in H_xNdNiO_3 and oxygen non-stoichiometry δ as in $NdNiO_{3-\delta}$) as a function of lateral position in the samples with a defect concentration gradient. Figure S10a shows the hydrogen non-stoichiometry x as a function of position in the sample with a proton concentration gradient, while Figure S10b shows the oxygen non-stoichiometry δ at different positions in the sample after thermochemical dehydration.

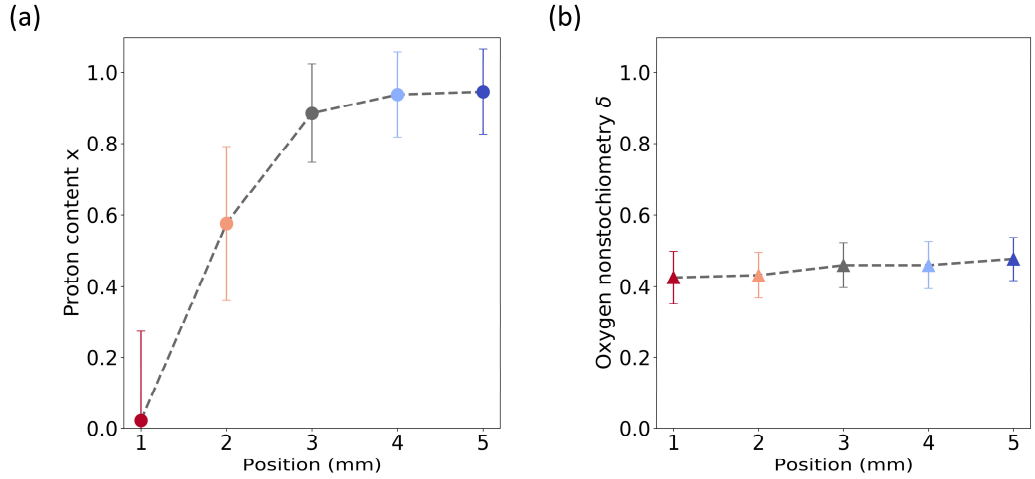

Figure S10 (a) Hydrogen non-stoichiometry x at different positions of a H_xNdNiO_3 thin film sample with proton concentration gradient. (b) Oxygen non-stoichiometry δ at a different position of a $NdNiO_{3-\delta}$ thin film sample with oxygen vacancy concentration gradient.

Ni $L_{2,3}$-edge and O *K*-edge sXAS of the hydrogen annealed sample

We synthesized the NNO-δ sample by annealing the sample with the proton concentration gradient in the pure H_2 atmosphere at 300ºC. The oxygen vacancy concentration remained homogenous across the thin film. The extra feature peak A' at 854 eV in Ni L_3-edge of oxygen deficient sample NNO-δ has been observed (Figure S11a). A similar extra feature peak has also been observed in the infinite layer $LaNiO_2$ or $NdNiO_2$[1,2]. A pre-edge peak in the O *K*-edge of oxygen deficient NNO-δ is visible, marked by a dashed line in Figure S10b. A similar pre-edge peak has been observed in $Nd_{0.8}Sr_{0.2}NiO_2$[2], $Nd_4Ni_3O_8$[3] and $Nd_6Ni_5O_{12}$[4]. The sXAS results indicate that the Ni valence state of the hydrogen annealed sample is mixed Ni^{+}/Ni^{2+}.

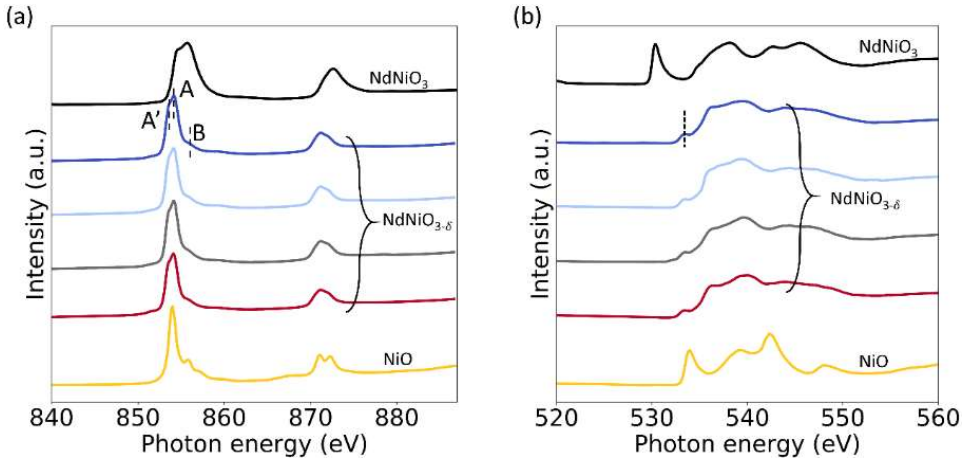

Figure S11. The sXAS of NNO-δ (a) Ni $L_{2,3}$-edge and (b) O *K*-edge.

The room-temperature conductivity of pristine $NdNiO_3$, protonated H_xNdNiO_3 and oxygen deficient $NdNiO_{3-\delta}$

As shown in Figure S12, it is the comparison between the room-temperature conductivity of $NdNiO_3$ samples with protons/oxygen vacancies and a pristine $NdNiO_3$ sample. We can see that the conductivity of $NdNiO_3$ samples with defects (either protons or oxygen vacancies) are orders of magnitude lower than that of the pristine $NdNiO_3$ sample.

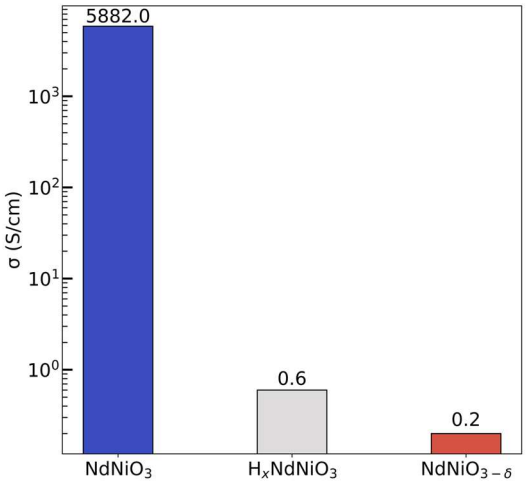

Figure S12. The room-temperature conductivity of pristine $NdNiO_3$, protonated H_xNdNiO_3, and oxygen deficient $NdNiO_{3-\delta}$.

References

(1) Hepting, M.; Li, D.; Jia, C. J.; Lu, H.; Paris, E.; Tseng, Y.; Feng, X.; Osada, M.; Been, E.; Hikita, Y.; Chuang, Y. D.; Hussain, Z.; Zhou, K. J.; Nag, A.; Garcia-Fernandez, M.; Rossi, M.; Huang, H. Y.; Huang, D. J.; Shen, Z. X.; Schmitt, T.; Hwang, H. Y.; Moritz, B.; Zaanen, J.; Devereaux, T. P.; Lee, W. S. Electronic Structure of the Parent Compound of Superconducting Infinite-Layer Nickelates. *Nat. Mater.* **2020**, *19* (4), 381–385.

(2) Goodge, B. H.; Li, D.; Lee, K.; Osada, M.; Wang, B. Y.; Sawatzky, G. A.; Hwang, H. Y.; Kourkoutis, L. F. Doping Evolution of the Mott-Hubbard Landscape in Infinite-Layer Nickelates. *Proc. Natl. Acad. Sci. U. S. A.* **2021**, *118* (2), 1–7.

(3) Ferenc Segedin, D.; Goodge, B. H.; Pan, G. A.; Song, Q.; LaBollita, H.; Jung, M. C.; El-Sherif, H.; Doyle, S.; Turkiewicz, A.; Taylor, N. K.; Mason, J. A.; N'Diaye, A. T.; Paik, H.; El Baggari, I.; Botana, A. S.; Kourkoutis, L. F.; Brooks, C. M.; Mundy, J. A. Limits to the Strain Engineering of Layered Square-Planar Nickelate Thin Films. *Nat. Commun.* **2023**, *14* (1), 1–14.

(4) Pan, G. A.; Ferenc Segedin, D.; LaBollita, H.; Song, Q.; Nica, E. M.; Goodge, B. H.; Pierce, A. T.; Doyle, S.; Novakov, S.; Córdova Carrizales, D.; N'Diaye, A. T.; Shafer, P.; Paik, H.; Heron, J. T.; Mason, J. A.; Yacoby, A.; Kourkoutis, L. F.; Erten, O.; Brooks, C. M.; Botana, A. S.; Mundy, J. A. Superconductivity in a Quintuple-Layer Square-Planar Nickelate. *Nat. Mater.* **2022**, *21* (2), 160–164.